



Reflective all-sky thermal infrared cloud imager

Brian J. Redman,^{1,2} Joseph A. Shaw,^{1,*} Paul W. Nugent,^{1,3} R. Trevor Clark,^{1,4} AND Sabino Piazzolla⁵

¹Electrical & Computer Engineering Department, Montana State University, Bozeman, MT 59717, USA

²Currently with the College of Optical Sciences, University of Arizona, Tucson, AZ 85721, USA

³Currently with NWB Sensors, Inc., 1716 W. Main St., Suite 8B, Bozeman, MT 59718, USA

⁴Currently with the Electromagnetics Team, Pacific Northwest National Laboratory, 902 Battelle Rd., Richland, WA 99352, USA

⁵Jet Propulsion Laboratory, California Institute of Technology, 4800 Oak Grove Dr. M/S 161-135, Pasadena, CA 91190, USA

*joseph.shaw@montana.edu

Abstract: A reflective all-sky imaging system has been built using a long-wave infrared microbolometer camera and a reflective metal sphere. This compact system was developed for measuring spatial and temporal patterns of clouds and their optical depth in support of applications including Earth-space optical communications. The camera is mounted to the side of the reflective sphere to leave the zenith sky unobstructed. The resulting geometric distortion is removed through an angular map derived from a combination of checkerboard-target imaging, geometric ray tracing, and sun-location-based alignment. A tape of high-emissivity material on the side of the reflector acts as a reference that is used to estimate and remove thermal emission from the metal sphere. Once a bias that is under continuing study was removed, sky radiance measurements from the all-sky imager in the 8-14 μm wavelength range agreed to within 0.91 $\text{W}/(\text{m}^2 \text{sr})$ of measurements from a previously calibrated, lens-based infrared cloud imager over its 110° field of view.

© 2018 Optical Society of America under the terms of the [OSA Open Access Publishing Agreement](#)

OCIS codes: (010.0280) Remote sensing and sensors; (010.1615) Clouds; (110.3080) Infrared imaging; (010.5630) Radiometry.

References and links

1. R. Bennartz, M. D. Shupe, D. D. Turner, V. P. Walden, K. Steffen, C. J. Cox, M. S. Kulie, N. B. Miller, and C. Pettersen, "July 2012 Greenland melt extent enhanced by low-level liquid clouds," *Nature* **496**(7443), 83–86 (2013).
2. J. M. Intrieri, M. D. Shupe, T. Uttal, and B. J. McCarty, "An annual cycle of arctic cloud characteristics observed by radar and lidar at SHEBA," *J. Geophys. Res.: Oceans* **107**, 1–15 (2002).
3. X. Dong, B. Xi, and P. Minnis, "A climatology of midlatitude continental clouds from the ARM SGP Central Facility. Part II: Cloud fraction and surface radiative forcing," *J. Clim.* **19**, 1765–1783 (2006).
4. R. D. Cess and P. M. Udelhofen, "Climate change during 1985-1999: Cloud interactions determined from satellite measurements," *Geophys. Res. Lett.* **30**(1), 1–4 (2003).
5. M. C. Wyant, M. Khairoutdinov, and C. S. Bretherton, "Climate sensitivity and cloud response of a GCM with a superparameterization," *Geophys. Res. Lett.* **33**(6), L06714 (2006).
6. J. Sabburg and J. Wong, "Evaluation of a ground-based sky camera system for use in surface irradiance measurement," *J. Atmos. Ocean. Technol.* **16**, 752–759 (1999).
7. G. Pfister, R. L. McKenzie, J. B. Liley, A. Thomas, and B. W. Forgan, "Cloud coverage based on all-sky imaging and its impact on surface solar irradiance," *J. Appl. Meteorol.* **42**, 1421–1434 (2003).
8. J. E. Shields, R. W. Johnson, M. E. Karr, A. R. Burden, and J. G. Baker, "Daylight visible/NIR whole sky imagers for cloud and radiance monitoring in support of UV research programs," in *Ultraviolet Ground- and Space-based Measurements, Models, and Effects III*, James R. Slusser and W. Gao, eds., *Proc. SPIE* **5156**, 155–166 (2003).
9. R. Tapakis and A. G. Charalambides, "Equipment and methodologies for cloud detection and classification: a review," *Sol. Energy* **95**, 392–430 (2013).
10. C. L. Hull, S. Limmongkol, and W. A. Siegmund, "Sloan digital sky survey cloud scanner," in *Advanced Technology Optical Telescopes V*, Larry, M. Stepp, eds., *Proc. SPIE* **2199**, 852–857 (1994).
11. A. Mallama and J. J. Degna, "A thermal infrared cloud-mapping instrument for observatories," *Publ. Astron. Soc. Pac.* **114**, 913–917 (2002).

12. N. Takato, N. Okada, G. Kosugi, M. Suganuma, A. Miyashita, and F. Ugauchi, "All-sky 10 μm cloud monitor on Mauna Kea," *Proc. SPIE* **4837**, 872–877 (2003).
13. A. Maghrabi, R. Clay, N. Wild, and B. Dawson, "Design and development of a simple infrared monitor for cloud detection," *Energy Convers. Manage.* **50**, 2732–2737 (2009).
14. P. W. Nugent, J. A. Shaw, and S. Piazzolla, "Infrared cloud imaging in support of Earth-space optical communication," *Opt. Express* **17**(10), 7862–7872 (2009).
15. P. W. Nugent, J. A. Shaw, and S. Piazzolla, "Infrared cloud imager development for atmospheric optical communication characterization, and measurements at the JPL Table Mountain Facility," IPN Progress Report 42–192, 1–31, http://tmo.jpl.nasa.gov/progress_report/42-192/192C.pdf (2013).
16. S. Piazzolla and S. Slobin, "Statistics of link blockage due to cloud cover for free-space optical communications using NCDC surface weather observation data," *Proc. SPIE* **4635**, 138–149 (2002).
17. D. M. Boroson, B. S. Robinson, D. V. Murphy, D. A. Burianek, F. Khatri, J. M. Kovalik, Z. Sodnik, and D. M. Cornwell, "Overview and results of the Lunar Laser Communication Demonstration," *Proc. SPIE* **8971**, 89710S (2014).
18. S. Poulenard, M. Ruellana, B. Roy, J. Riédi, F. Parol, and A. Rissons, "High altitude clouds impacts on the design of optical feeder link and optical ground station network for future broadband satellite services," *Proc. SPIE* **8971**, 897107 (2014).
19. B. D. Felton, P. D. Hayes, and R. J. Alliss, "Improved atmospheric characterization for free-space link analysis using numerical weather prediction," *Proc. SPIE* **8380**, 83800C (2012).
20. C. N. Long, J. M. Sabburg, J. Calbó, and D. Pagès, "Retrieving cloud characteristics from ground-based daytime color all-sky images," *J. Atmos. Ocean. Technol.* **23**, 633–652 (2006).
21. M. C. Allmen and W. Philip Kegelmeyer, Jr., "The computation of cloud-base height from paired whole-sky imaging cameras," *J. Atmos. Ocean. Technol.* **13**, 97–113 (1996).
22. J. Shaw, P. Nugent, N. Pust, B. Thurairajah, and K. Mizutani, "Radiometric cloud imaging with an uncooled microbolometer thermal infrared camera," *Opt. Express* **13**(15), 5807–5817 (2005).
23. J. A. Shaw, P. W. Nugent, N. J. Pust, B. J. Redman, and S. Piazzolla, "Cloud optical depth measured with ground-based uncooled infrared imagers," *Proc. SPIE* **8523**, 85231D (2012).
24. J. E. Shields, M. E. Karr, R. W. Johnson, and A. R. Burden, "Day/night whole sky imagers for 24-h cloud and sky assessment: history and overview," *Appl. Opt.* **52**(8), 1605–1616 (2013).
25. A. Kazantzidis, P. Tzoumanikas, A. F. Bais, S. Fotopoulos, and G. Economou, "Cloud detection and classification with the use of whole-sky ground-based images," *Atmos. Res.* **113**, 80–88 (2012).
26. K. McGuffie and A. Henderson-Sellers, "Almost a century of 'imaging' clouds over the whole-sky dome," *Bull. Am. Meteorol. Soc.* **70**, 1243–1253 (1989).
27. G. Horváth, A. Barta, J. Gál, B. Suhai, and O. Haiman, "Ground-based full-sky imaging polarimetry of rapidly changing skies and its use for polarimetric cloud detection," *Appl. Opt.* **41**(3), 543–559 (2002).
28. N. J. Pust and J. A. Shaw, "Dual-field imaging polarimeter using liquid crystal variable retarders," *Appl. Opt.* **45**(22), 5470–5478 (2006).
29. N. J. Pust and J. A. Shaw, "Digital all-sky polarization imaging of partly cloudy skies," *Appl. Opt.* **47**(34), H190–H198 (2008).
30. A. Kreuter, M. Zangerl, M. Schwarzmann, and M. Blumthaler, "All-sky imaging: a simple, versatile system for atmospheric research," *Appl. Opt.* **48**(6), 1091–1097 (2009).
31. A. Cazorla, F. J. Olmo, and L. Alados-Arboledas, "Development of a sky imager for cloud cover assessment," *J. Opt. Soc. Am. A* **25**(1), 29–39 (2008).
32. D. I. Klebe, R. D. Blatherwick, and V. R. Morris, "Ground-based all-sky mid-infrared and visible imagery for purposes of characterizing cloud properties," *Atmos. Meas. Tech.* **7**, 637–645 (2014).
33. P. W. Nugent, J. A. Shaw, and N. J. Pust, "Correcting for focal-plane-array temperature dependence in microbolometer infrared cameras lacking thermal stabilization," *Opt. Eng.* **52**(6), 061304 (2013).
34. P. W. Nugent, J. A. Shaw, and N. J. Pust, "Radiometric calibration of infrared imagers using an internal shutter as an equivalent external blackbody," *Opt. Eng.* **53**(12), 123106 (2014).
35. P. W. Nugent and J. A. Shaw, "Calibration of uncooled LWIR microbolometer imagers to enable long-term field deployment," *Proc. SPIE* **9071**, 90710V (2014).
36. B. Thurairajah and J. A. Shaw, "Cloud statistics measured with the infrared cloud imager (ICI)," *IEEE Trans. Geosci. Remote Sens.* **43**, 2000–2007 (2007).
37. J. A. Shaw and P. W. Nugent, "Physics principles in radiometric infrared imaging of clouds in the atmosphere," *Eur. J. Phys.* **34**, 111 (2013).
38. E. Kassianov, C. N. Long, and M. Ovtchinnikov, "Cloud sky cover versus cloud fraction: whole-sky simulations and observations," *J. Appl. Meteorol.* **44**(1), 86–98 (2005).
39. Z. Zhang, "A Flexible New Technique for Camera Calibration," *IEEE Trans. Pattern Anal. Mach. Intell.* **22**, 1330–1334 (2000).
40. M. Vo, Z. Wang, L. Luu, and J. Ma, "Advanced geometric camera calibration for machine vision," *Opt. Eng.* **50**, 110503 (2011).
41. D. W. Riesland, "Infrared cloud imaging systems characterization," M.S. Thesis (Optics & Photonics), Montana State University, <http://scholarworks.montana.edu/xmlui/handle/1/12381> (2016).

1. Introduction

Spatial and temporal cloud statistics are important in studies of climate [1–5], solar radiation [6–9], astronomy [10–13], and earth-space optical communications [14–19]. For these needs, autonomous imaging systems have been developed to make measurements of parameters such as the fraction of the sky that is cloudy [20], cloud height [21], cloud emissivity [22], and cloud optical depth [23,24]. Ground-based infrared imaging systems are particularly well suited to addressing these needs with day and night consistency and high temporal resolution.

All-sky imaging systems have used either reflective optics or fisheye lenses [24–26], and a variety of data-processing techniques that include radiometric images of daylight and starlight [24], visible-wavelength ratios [20,25], polarimetry [27–30], and neural networks [31]. In addition to the most common visible and near-infrared (VNIR) cloud imagers, long-wave infrared (LWIR) systems are being developed with the advantage of providing equal day and night sensitivity with the same cloud retrieval algorithm, as long as clear-air emission is properly estimated and removed (this is done primarily with an estimate of atmospheric water vapor, but does not vary with aerosols [37]). Single-pixel infrared sensors have been used to scan the sky [10,13], but the advent of uncooled microbolometers has enabled all-sky infrared imaging using reflective optics [11,12] and fisheye lenses [32].

Our Infrared Cloud Imager (ICI) systems are based on uncooled thermal imagers that combine microbolometer detectors with advanced radiometric calibration algorithms [14,15,33–35] and radiometric image processing to compensate for the atmosphere and calculate cloud fraction and products such as cloud emissivity, optical depth, and attenuation [14,15,23,36,37]. This paper describes a reflective all-sky Infrared Cloud Imager (ICI) system that uses a metal sphere to reflect the full sky into a low-cost, weather-proof microbolometer camera positioned off axis to allow for an unobstructed view of the zenith sky. Although a 100° full-angle field of view is good for studying clouds in climate [38], all-sky coverage is preferred for monitoring and predicting clouds in earth-space optical communications [17–19]. We also have developed lens-based ICI systems with fields of view from narrow to all-sky, but the reflective system was developed for all-sky imaging at a small fraction of the cost of a thermal infrared fisheye lens. We describe the reflective all-sky ICI system and data processing and then compare data from it and a previously validated, lens-based ICI system.

2. Instrument layout and calibration

2.1 Instrument layout

The reflective all-sky imager positions a low-cost FLIR PathfindIR camera, a weatherproof microbolometer camera designed for automotive use (320 × 240 pixels, 36° × 27° field of view, 8–14 μm wavelength range), to the side of a 10-cm-diameter aluminum sphere serving as a low-cost reflector, as shown in Fig. 1. The off-axis design prevents obstructions within 60° of zenith to allow comparison with zenith-viewing instruments and to maximize use of the angular region where atmospheric models are most accurate. The off-axis geometry leads to distortion that is removed in image processing described later. The corrected images see approximately 95% of the full sky. The system can be positioned with the arm pointing in any desired direction.

2.2 Radiometric calibration

The infrared camera was calibrated using methods developed at Montana State University for achieving stable, radiometrically calibrated output from microbolometer cameras [33–35]. Additionally, the sphere reflectivity and emissivity were determined for each pixel of the all-sky image by using a scanning telescope mount to rotate the sphere in front of a large-area blackbody calibration source at different blackbody temperatures and at different sphere temperatures (rotating the sphere was much easier than rotating the heavy blackbody source).

The resulting data were used to solve for the reflectivity and emissivity of the sphere as a function of location, which was then mapped to each pixel of the all-sky imager.



Fig. 1. The reflective all-sky ICI uses an aluminum sphere to reflect the whole sky into a low-cost LWIR camera in an off-axis position to avoid blocking the zenith sky.

2.3 Removing sphere emission

One of the functions of the all sky cloud imager is to derive the sky radiance (L_{sky}) from the overall radiance measured in the reflected image (L_m), which also includes radiance emitted by the sphere itself ($\epsilon_s L_{bb}(T)$) for sphere emissivity ϵ_s and blackbody radiance L_{bb} at reflector temperature T . The radiance measured at a pixel of indices i and j can be written as a sum of the reflected and emitted components:

$$L_m(i, j) = [1 - \epsilon_s(i, j)] L_{sky}(i, j) + \epsilon_s(i, j) L_{bb}(T). \quad (1)$$

The sphere-emitted radiance denoted by the second term on the right-hand side of this equation was determined using laboratory measurements of the emissivity at each point on the sphere at the angles seen by the camera. However, for simplicity, rather than trying to directly measure the sphere temperature, we calculated $L_{bb}(T)$ from real-time measurements of a small reference target. This reference was a small strip of tape of emissivity $\epsilon_{ref} = 0.97$, attached to the sphere within the camera's FOV but in a region where the sky view was obscured by the arm supporting the infrared camera, as shown in Fig. 1.

The procedure for deriving the $L_{bb}(T)$ term was as follows. First, we expressed the radiance measured in the reference region as

$$L_{ref} = (1 - \epsilon_{ref}) L_{bg} + \epsilon_{ref} L_{bb}(T), \quad (2)$$

where L_{bg} is the background radiance seen by the reference region of the sphere. Next, we solved Eq. (2) for the desired radiance term,

$$L_{bb}(T) = \frac{L_{ref} - (1 - \epsilon_{ref}) L_{bg}}{\epsilon_{ref}}. \quad (3)$$

At this point the L_{bg} term was still unknown, but a good approximation of L_{bg} could be found iteratively using the average of L_{sky} for all sky-viewing pixels. Determination of the average L_{sky} was done in an iterative fashion, deriving first L_{bb} by setting L_{bg} to zero in Eq. (3), then calculating the average L_{sky} as

$$\widehat{L}_{bg} \equiv \overline{L_{sky}(i,j)} = \frac{\overline{L_m(i,j) - \epsilon_s(i,j)L_{bb}(T)}}{1 - \overline{\epsilon_s(i,j)}}. \quad (4)$$

Using \widehat{L}_{bg} from Eq. (3) to again derive $L_{bb}(T)$ and repeating it provided values of $L_{bb}(T)$ within the calibration uncertainty after just one iteration. Finally, this iterative estimate of $L_{bb}(T)$ was used to derive the sky radiance for each pixel,

$$L_{sky}(i,j) = \frac{L_m(i,j) - \epsilon_s(i,j)L_{bb}(T)}{1 - \epsilon_s(i,j)}. \quad (5)$$

All these processing steps were done in real time by a computer that communicated with the ICI system while displaying a real-time image of sky radiance.

2.4 Angle mapping

Accurate characterization of clear-sky emission in the image processing required that we calculate the pointing angle of each pixel. The first step in accomplishing this was to measure the angular pointing for each camera pixel (without the sphere but with the lens) using images of a checkerboard pattern to determine lens distortion with the Camera Calibration Toolbox for MATLAB [39-40]. The toolbox routines were designed for use with visible images, but we extended their application to the thermal infrared by using a lamp as a source to apply heat to the checkerboard so that the black areas emitted more brightly than white ones.

Next, we derived the zenith angles in the sky for each pixel of the complete system (including reflection from the sphere). This was done with geometric ray tracing from each camera pixel to the sphere and reflecting from there into the sky, assuming a perfectly spherical reflector surface. A final post-processing alignment was achieved by comparing the measured position of the sun over a period of several days to the calculated solar zenith and azimuth angles and solving for the rotation of the measured sky image to minimize the error between the recorded and calculated solar positions. Figure 2 shows the zenith angles for each pixel mapped onto the reflective sphere (with a black line denoting the location of the horizon). These reflected angle maps were used to determine the instantaneous field of view (IFOV) solid angle for each pixel by calculating the fraction of the overlying 2π -sr hemisphere seen by each pixel.

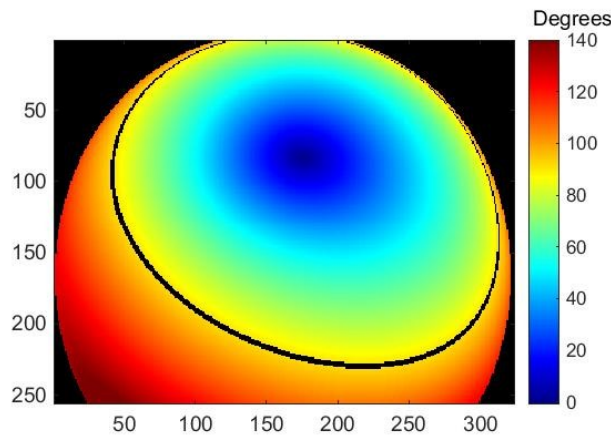


Fig. 2. The IR camera's view of the sphere, showing the zenith angle for each pixel after reflection. The black line indicates the location of the horizon.

3. Results

With a few modifications to extend the models to larger zenith angles, the reflective all-sky ICI used the same algorithms as previous infrared cloud imaging systems to detect clouds and estimate their optical depth [14,15,23]. Figure 3 shows sky images at three different points in the processing. Raw images were calibrated to produce sky radiance images as in Fig. 3(a). This initial image was processed to obtain equal-angle sky projection, as in Fig. 3(b). Finally, the corrected sky radiance images were used to derive the cloud optical depth according to the approach described in [14,15,23], as shown in Fig. 3(c). A mask also was applied to this image to remove obstructions such as buildings, mountains, and the off-zenith camera obstruction. [Visualization 1](#) (Fig. 4) shows radiance and cloud optical depth for a variety of cloud conditions measured on 22 June 2012.

Data from the reflective all-sky ICI were validated with another calibrated infrared cloud imager (the third-generation ICI or ICI3). The ICI3 is a lens-based cloud imager system with a diagonal FOV of 110° [23]. For this comparison, the two systems were operated together for a period of twenty-five days in May-June 2012 at Montana State University. Sky images from the reflective all-sky ICI were cropped to match the ICI3's 110° FOV after both systems were aligned using a sun-based alignment method to within approximately two pixels ($\sim 2^\circ$) on the reflective all-sky ICI. Figure 5 shows an example pair of sky images from the ICI3 and the reflective all-sky ICI with the latter interpolated to remove distortion and cropped to match the ICI3 field of view (the obstruction appears in the upper-left corner of the reflective image because of the different instrument locations, not because of mismatched FOV).

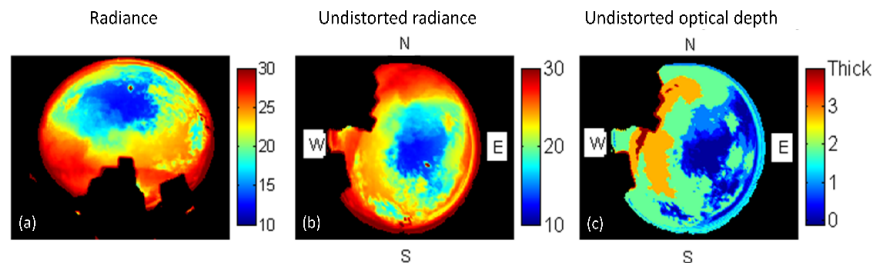


Fig. 3. Example images at three levels of processing: (a) radiance image [$\text{W}/(\text{m}^2 \text{sr})$] with geometric distortion induced by the off-axis reflection; (b) radiance image undistorted and remapped into an equal-angle projection with north at the top; and (c) cloud optical depth ("thick" means cloud optical depth exceeding 4). The black regions within the circular image mask obstructions by buildings, mountains, and the camera.

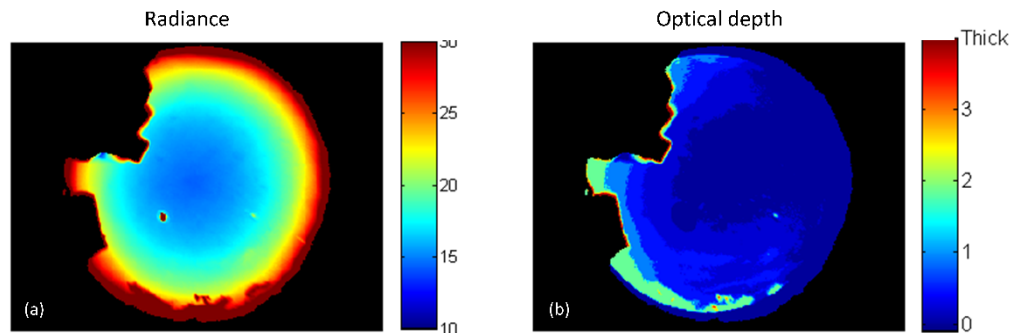


Fig. 4. [Visualization 1](#) shows images taken once per minute for 15 hours and played back at 15 frames per second, showing (a) sky and cloud radiance and (b) cloud optical depth. The circle that moves across the image starting at 0:36 is where the Sun was removed by software.

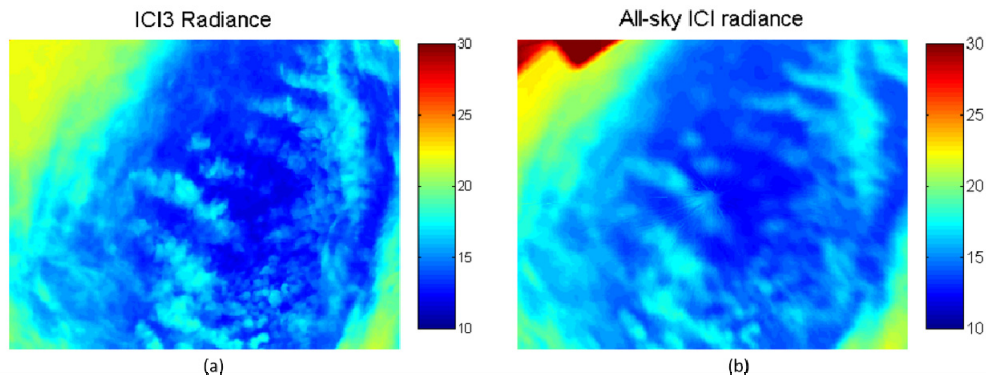


Fig. 5. Sky radiance [$\text{W}/(\text{m}^2 \text{sr})$] measured in a common field of view by (a) the ICI3 and (b) the reflective all-sky ICI (camera obstruction appears as dark red area in upper-left corner).

Figure 6(a) is a scatterplot comparing the frame-averaged sky radiance in the overlapping region of the two imagers (with the obstructions removed). There is a small gain bias (1.06 vs. 1.00) and a modest offset (2.48 $\text{W}/(\text{m}^2 \text{sr})$). The offset could result from the unknown spectral transmission of the camera's optical window, uncertainties in the reference tape emissivity and sphere reflectance over time, nonuniform solar heating of the sphere, or calibration drift of the PathfindIR camera, but almost certainly includes uncertainties in the PathfindIR spectral response function [41]. There was no correlation found for the offset with either solar irradiance or ambient temperature. After the data from the reflective all-sky ICI were reprocessed using a gain and offset correction based on the trend, data from the two imagers exhibited a standard deviation of 0.91 $\text{W}/(\text{m}^2 \text{sr})$ and the sky radiance differences were approximately normally distributed, as shown in Fig. 6(b), indicating effective removal of systematic errors.

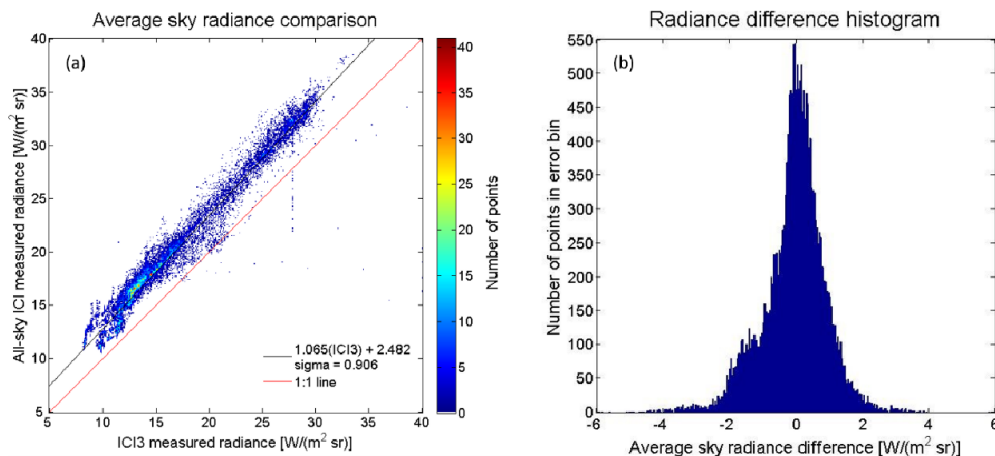


Fig. 6. (a) Scatterplot of radiance averaged over the common FOV of the ICI3 and the reflective all-sky ICI for 25 days; (b) histogram of frame-averaged sky radiance differences after gain and offset correction.

Figure 7 shows a five-day comparison of the spatially averaged sky radiance measured by the reflective all-sky imager and the ICI-3 in their common field of view, with the systematic bias removed. These measurements were obtained during a subsequent deployment of the system during 3-7 March 2017 at Montana State University in Bozeman, Montana. There are some differences that are worthy of further study, but they both show a very similar radiance

pattern, which helps confirm that the reflective ICI can produce data that compare reasonably well with the more sophisticated and controlled ICI-3 instrument.

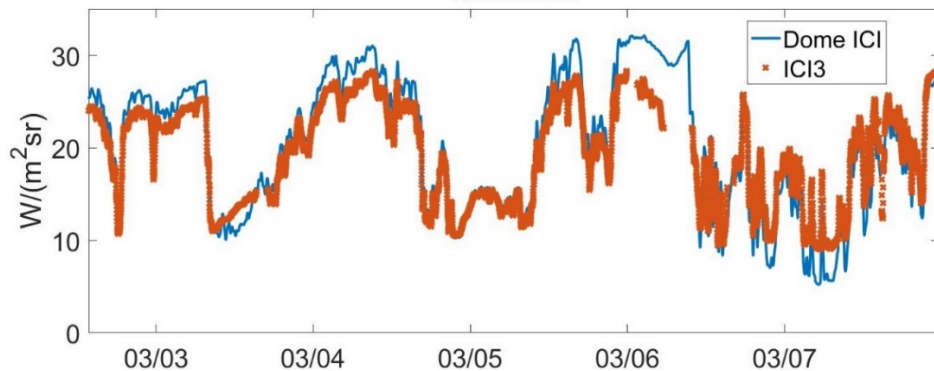


Fig. 7. Time-series plot of the spatially averaged sky radiance from the reflective ICI and the ICI-3 instrument for 3-7 March 2017 at Montana State University in Bozeman, Montana (Mountain Standard Time = UTC - 7 hours).

4. Conclusions

A compact and low-cost system was developed to achieve long-wave infrared all-sky imaging for consistent day-night imaging of clouds in the atmosphere. The system uses a reflective metal sphere with an uncooled microbolometer camera positioned to one side to leave an unobstructed zenith sky. The off-zenith camera position introduces asymmetry that generates unevenly distributed distortion, which has been compensated using an angular map derived from a combination of geometric ray tracing and checkerboard-target imaging. A painted strip on the side of the sphere provides a reference of known high emissivity from which sphere emission is estimated and removed. The entire system makes use of calibration methods that enable accurate radiometric measurements from uncooled thermal cameras through continuous compensation of the changing camera response. Sky radiance measurements from the reflective all-sky imager agreed to within $0.91 W/(m^2 sr)$ of simultaneous measurements from a previously validated infrared cloud imager after we removed a systematic bias. Since the camera calibration method has been demonstrated elsewhere to remain accurate in long-term field deployments, we suspect the origin of this bias to be associated with uncertainties in the camera spectral response function, the spectral transmission of the window over the camera, changes in the reference tape emissivity and sphere reflectivity, or nonuniform solar heating of the sphere. These are all subjects of continued study.

Funding

National Science Foundation (NSF) (ARC-1108427); Air Force Office of Scientific Research (AFOSR) (FA9550-14-1-0140); Montana Space Grant Consortium (MSGC).

Acknowledgments

Portions of this research were carried out at the Jet Propulsion Laboratory, California Institute of Technology, under a contract with the National Aeronautics and Space Administration. The views and conclusions contained herein are those of the authors and should not be interpreted as necessarily representing the official policies or endorsements, either expressed or implied, of NASA, the Air Force Research Laboratory, or the U.S. Government.